A new estimator for directional properties of nearshore waves

A. Sheremet[1]
Coastal Studies Institute, Louisiana State University, Baton Rouge, Louisiana, USA

R. T. Guza
Integrative Oceanography Division, Scripps Institution of Oceanography, University of California, San Diego, La Jolla, California, USA

T. H. C. Herbers
Department of Oceanography, Naval Postgraduate School, Monterey, California, USA

Received 5 December 2003; revised 16 August 2004; accepted 18 November 2004; published 4 January 2005.

[1] The infragravity wave (periods between roughly 20 and 200 s) energy balance in shallow, nearshore waters is believed to be effected by generation by groups of sea and swell, dissipation, shoreline reflection, and refractive trapping. Observations obtained with alongshore oriented arrays of current meters or pressure gauges have been previously used to identify concentrations of energy at the frequency-alongshore wavenumbers of refractively trapped edge waves, but seaward and shoreward propagating waves were not differentiated. Surfzone dissipation theoretically limits edge wave growth, and a different analysis (using the approximation of shore-normal propagation) shows that the energy flux of shoreward propagating infragravity waves decreases owing to surfzone dissipation. Here an estimator is developed that yields the alongshore wavenumber-frequency spectra of seaward and shoreward propagating waves, using the WKB approximation and observations from an alongshore-oriented array of pressure and velocity sensors. Example spectra, estimated using data from the spatially sparse and relatively short SandyDuck arrays, suggests that strong dissipation of shoreward propagating infragravity waves occurs over a wide range of alongshore wavenumbers, effectively suppressing the excitation of edge wave modes.

Citation: Sheremet, A., R. T. Guza, and T. H. C. Herbers (2005), A new estimator for directional properties of nearshore waves, *J. Geophys. Res.*, *110*, C01001, doi:10.1029/2003JC002236.

1. Introduction

[2] Infragravity waves, with periods (between roughly 20 and 200 s) longer than sea and swell (between about 2–20 s), are ubiquitous on ocean shorelines. Generation by groups of sea and swell, dissipation, shoreline reflection, and refractive trapping have all been suggested to contribute significantly to the infragravity energy balance in shallow, nearshore waters [e.g., *Munk*, 1949; *Longuet-Higgins and Stewart*, 1962; *Gallagher*, 1971; *Suhayda*, 1974; *Huntley et al.*, 1981; *Herbers et al.*, 1995a, 1995b; *Ruessink*, 1998; *Henderson and Bowen*, 2002, 2003; *Janssen and Battjes*, 2003; *Battjes et al.*, 2004]. A new method is presented here for analyzing the wave energy balance using array measurements of pressure and velocity.

[3] Some earlier studies of the infragravity energy balance assumed approximately shore-normal propagating long waves. In this approximation, collocated observations of pressure (p) and cross-shore velocity (u) can be combined to estimate the time series of sea surface elevation associated with shoreward and seaward propagating waves ($\eta_{\pm}$, respectively)

$$\eta_{\pm} = \frac{1}{2}\left(p \pm u\sqrt{h/g}\right), \tag{1}$$

where h is the depth and g is gravitational acceleration [e.g., *Guza et al.*, 1984; *Elgar and Guza*, 1985; *List*, 1992]. Frequency spectra of shoreward and seaward directed energy fluxes can be expressed as functions of the p, u auto- and cross-spectra. A case example from the SandyDuck experiment (Figure 1), conducted on a straight, gently sloped beach near Duck, North Carolina, shows the expected significant decrease in shoreward sea-swell energy flux within the surf zone (Figure 2a, x less than $\sim$230 m), and low energy levels of seaward

[1] Also at Department of Oceanography and Coastal Sciences, Louisiana State University, Baton Rouge, Louisiana, USA.

0148-0227/05/2003JC002236$09.00

Report Documentation Page

Form Approved
OMB No. 0704-0188

1. REPORT DATE	2. REPORT TYPE	3. DATES COVERED
2005		**00-00-2005 to 00-00-2005**

4. TITLE AND SUBTITLE	5a. CONTRACT NUMBER
A New Estimator for Directional Properties of Nearshore Waves	5b. GRANT NUMBER
	5c. PROGRAM ELEMENT NUMBER
6. AUTHOR(S)	5d. PROJECT NUMBER
	5e. TASK NUMBER
	5f. WORK UNIT NUMBER
7. PERFORMING ORGANIZATION NAME(S) AND ADDRESS(ES) **Coastal Studies Institute,Louisiana State University,Baton Rouge,LA**	8. PERFORMING ORGANIZATION REPORT NUMBER
9. SPONSORING/MONITORING AGENCY NAME(S) AND ADDRESS(ES)	10. SPONSOR/MONITOR'S ACRONYM(S)
	11. SPONSOR/MONITOR'S REPORT NUMBER(S)

12. DISTRIBUTION/AVAILABILITY STATEMENT
Approved for public release; distribution unlimited

13. SUPPLEMENTARY NOTES

14. ABSTRACT

15. SUBJECT TERMS

16. SECURITY CLASSIFICATION OF:			17. LIMITATION OF ABSTRACT	18. NUMBER OF PAGES	19a. NAME OF RESPONSIBLE PERSON
a. REPORT **unclassified**	b. ABSTRACT **unclassified**	c. THIS PAGE **unclassified**	**Same as Report (SAR)**	**11**	

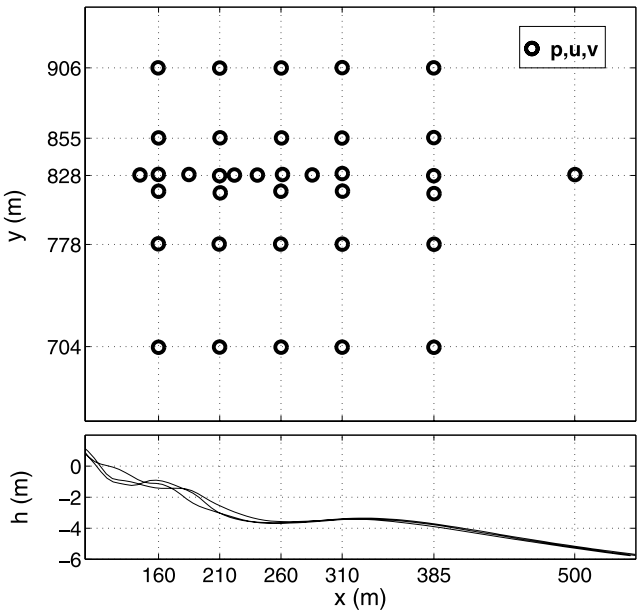

Figure 1. (top) Plan view of SandyDuck instrument array [*Feddersen et al.*, 2000; *Elgar et al.*, 2001]. Collocated pressure (p) and horizontal velocity (u, v) sensors are indicated (instruments were occasionally nonfunctional). The Field Research Facility coordinate frame is used, with x and y the cross-shore and alongshore directions. (bottom) Depth relative to MSL versus x is similar in August, September, and November (solid curves). The x origin is a fixed onshore point, so the location of the mean shoreline varied with tide level and wave conditions.

propagating sea-swell waves. In contrast, the shoreward infragravity wave energy flux first increases (consistent with trapping and/or generation, Figure 2b) followed by a decrease in the inner surf zone (suggesting dissipation). A significant fraction of the shoreward infragravity energy reaches the shoreline and is strongly reflected, resulting in a mix of progressive and standing waves at all cross-shore locations (Figure 2c).

[4] Cross-shore patterns of energy flux variation qualitatively similar to Figure 2 are observed often during the SandyDuck experiment [*Sheremet et al.*, 2002]. Phase differences between pressure (or cross-shore velocity) observed at different cross-shore locations also suggest that sea-swell waves are predominantly shoreward progressive whereas infragravity waves are a mix of standing and shoreward progressive waves [*Henderson and Bowen*, 2002; *Sheremet et al.*, 2002].

[5] Alongshore wavenumber-frequency ($\kappa - f$) spectra of p, u, or v (v is the alongshore velocity) often have been estimated using coherent analysis of observations obtained with an alongshore-oriented linear array [e.g., *Munk et al.*, 1964]. The $\kappa - f$ spectra of p estimated using the MEM (Maximum Entropy Method, Figure 3a), is elevated at $f < 0.02$ Hz for κ within the theoretical range of low mode (<5) edge waves (Figure 3a). Edge waves, the normal modes of gravity waves undergoing complete, multiple reflections between the shoreline and the turning point (where $|\kappa| = \kappa_g = f/\sqrt{gh}$) have been hypothesized to be preferentially excited relative to $\kappa - f$ modes that are off the edge wave dispersion curve [*Gallagher*, 1971]. Indeed, previous observations of alongshore velocity close to the shoreline sometimes show concentrations of energy at the $\kappa - f$ of low mode edge waves [*Huntley et al.*, 1981; *Oltman-Shay and Guza*, 1987]. Dissipation at edge wave $\kappa - f$ theoretically reduces their resonant excitation [*Henderson and Bowen*, 2003], and the analysis using individual collocated p, u pairs (Figures 2b and 2c) suggests that a significant fraction of the shoreward propagating infragravity energy flux is dissipated.

[6] Two-dimensional arrays can provide estimates of the seaward and shoreward energy fluxes of directionally spread waves, but most existing methods assume a spatially homogeneous wave field [*Elgar et al.*, 1994; *Herbers et al.*, 1995b]. Inhomogeneity associated with phase coupling of seaward and shoreward propagating waves (standing wave patterns) can be neglected only if the array is located sufficiently far offshore of any reflector (e.g., the shoreline). This condition is often violated in surfzone experiments where measurements are collected within a few hundred meters of the shoreline. Phase-coupling between shoreward progressing and reflected waves is accounted for in the

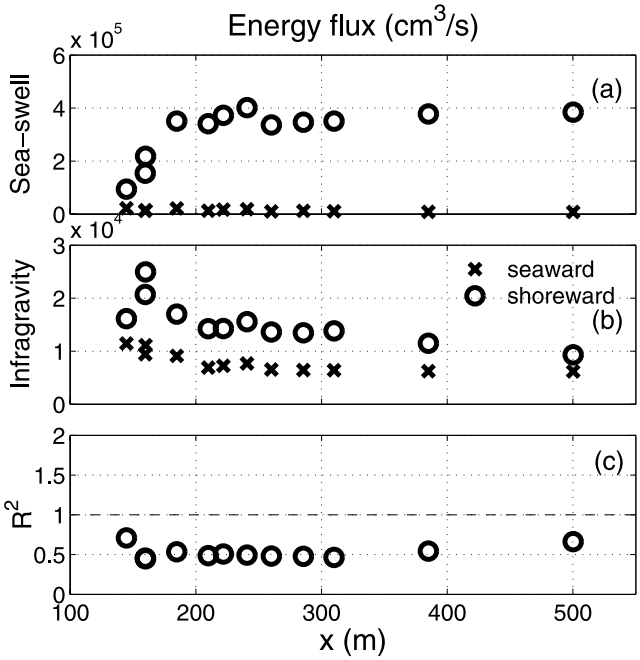

Figure 2. Results for 10 September 1997, 0100–0400 EST (Eastern Standard Time). The incident sea-swell peak period was about 12 s, with significant height of about 1 m. Assuming near-normal incidence (1), p and u sensors collocated at cross-shore locations along y = 828 m (Figure 1) are used to estimate frequency-band integrated seaward and shoreward energy fluxes for (a) sea swell (0.05–0.30 Hz), and (b) infragravity (0.01–0.05 Hz) waves. (c) Infragravity flux reflection coefficients (ratio of seaward to shoreward flux). (An erroneous date was given in the caption of Figure 3 [*Sheremet et al.*, 2002]. The data presented in the group of panels on the right of that figure were collected on 12 October 1997, 1300–1600 EST.)

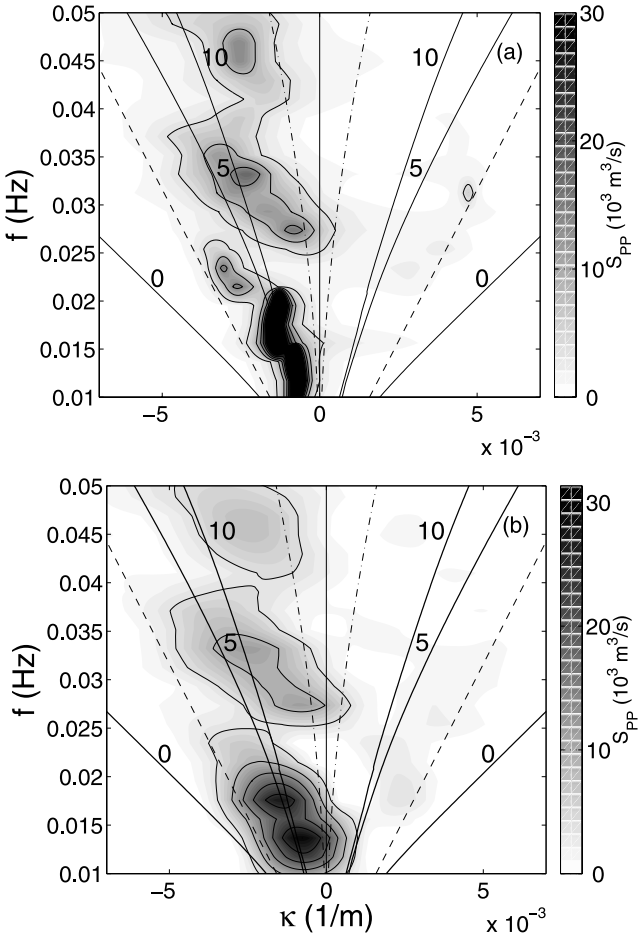

Figure 3. Alongshore wavenumber-frequency ($\kappa - f$) infragravity pressure spectra S_{PP}, for 10 September 1997 (0100–0400 EST), using the alongshore array of p sensors at x = 260 m (Figure 1) and (a) Maximum Entropy Method [*Wu*, 1997], and (b) new Hermite expansion method. Solid curves are edge wave dispersion relations for modes 0, 5, and 10, and dashed curves define turning points in the WKB approximation ($|\kappa| = \kappa_g = f/\sqrt{gh}$) that separate oscillatory and exponentially decaying cross-shore variations. The dash-dotted curves $\kappa = 2\pi f^2/g$ separate trapped from leaky waves, assuming deep water offshore. Pressure time series (3 hours long) were sampled at 2 Hz, quadratically detrended, divided into 448-s-long demeaned ensembles with 50% overlap, and each ensemble was tapered with a Hanning window, yielding cross-spectra with about 48 degrees of freedom and frequency resolution of 0.002 Hz.

estimators of *Isobe and Kondo* [1984], but this method is designed for two-dimensional arrays of pressure gauges in uniform water depth.

[7] Here a method is developed that yields estimates of $\kappa - f$ spectra of shoreward and seaward energy fluxes in the $\kappa - f$ region of (theoretically) refractively trapped infragravity waves. An extension of an existing method for a single $p - u$ gauge, the estimator uses the WKB approximation and observations from an alongshore (on a constant depth contour) array of $p - u$ gauges (Figure 1). The estimates are independent of phase-coupling between shoreward and seaward propagating waves. A few example spectra, estimated using data from the spatially sparse and relatively short SandyDuck arrays, suggest that dissipation of shoreward propagating infragravity waves occurs over a wide range of alongshore wavenumbers, including those of (theoretically) refractively trapped edge waves.

2. Cross-Shore Energy Fluxes in $\kappa - f$ Space

[8] The net cross-shore flux F of linear waves across a vertical section of unit width, oriented perpendicular to the wave propagation direction, is equal to the time-averaged (overbar), vertically integrated covariance of p and u [e.g., *Stoker*, 1947],

$$F = \overline{\int_{-h}^{0} pu\,dz}, \tag{2}$$

where for the long waves considered here, p and u are independent of the vertical coordinate z.

[9] With P, U, and V the double Fourier-Stieltjes transform from (x, y, t) space to (x, κ, f) space, of pressure, cross-shore, and alongshore velocities, for example,

$$p(x,y,t) = \int_{-\infty}^{\infty}\int_{-\infty}^{\infty} e^{2\pi i(\kappa y + ft)}\,dP(x,\kappa,f), \tag{3}$$

the distributions of the variances and covariance of p, u, and pu in $\kappa - f$ space are

$$\begin{aligned} S_{PP}\,df d\kappa &= 2\mathsf{E}\left[|dP|^2\right], \\ S_{UU}\,df d\kappa &= 2\mathsf{E}\left[|dU|^2\right], \\ S_{PU}\,df d\kappa &= 2\mathsf{E}[dP dU^*], \end{aligned} \tag{4}$$

where E [ ] denotes the expected value, and the factor 2 arises from folding negative onto positive frequencies. The $\kappa - f$ spectral densities of pressure and cross-shore velocity (S_{PP} and S_{UU}) are real and positive, whereas the cross-spectrum S_{PU} is complex.

[10] The $\kappa - f$ spectra (4), that can be estimated with an alongshore array of $p - u$ gauges (section 3), can be combined into expressions for the distribution of wave energy and energy flux in the four quadrants defined by the shore-seaward and up-down coast directions. Assume a directionally spread wave field composed of onshore and offshore propagating WKB long waves [e.g., *Herbers et al.*, 1995a, 1995b; *Sheremet et al.*, 2002],

$$dP(x,\kappa,f) = \frac{1}{2}\left[A_+(x,\kappa,f)\,e^{i\theta_+(x,\kappa,f)} + A_-(x,\kappa,f)\,e^{i\theta_-(x,\kappa,f)}\right], \tag{5}$$

where $A_\pm$ are the slowly varying, complex, local amplitude of shoreward (+) and seaward (−) propagating modes. Phase changes associated with propagation between the array location and the shoreline, and back to the array, are incorporated into the phase functions $\theta_\pm$.

[11] Using (5) and the WKB relationship between pressure and horizontal velocities $U = -(ig/f) \cdot \partial P/\partial x$ yields

$$S_{PP}\, d\kappa df = \mathsf{E}\left[\frac{1}{2}\left[|A_+|^2 + |A_-|^2 + 2\mathcal{R}e\left\{A_+ A_-^* e^{i(\theta_+ - \theta_-)}\right\}\right]\right], \tag{6}$$

$$S_{UU}\, d\kappa df = \mathsf{E}\left[\frac{C_x^2}{2h^2}\left[|A_+|^2 + |A_-|^2 - 2\mathcal{R}e\left\{A_+ A_-^* e^{i(\theta_+ - \theta_-)}\right\}\right]\right], \tag{7}$$

$$S_{PU}\, d\kappa df = \mathsf{E}\left[\frac{|C_x|}{2h}\left[|A_+|^2 + |A_-|^2 - 2i\mathcal{I}m\left\{A_+ A_-^* e^{i(\theta_+ - \theta_-)}\right\}\right]\right], \tag{8}$$

where the superscript asterisk indicates complex conjugate, $\mathcal{R}e$ and $\mathcal{I}m$ are the real and imaginary part of a complex variable, and the (x, κ, f) dependence of A, C_x, and θ are dropped for brevity. C_x and C_y are the cross-shore and alongshore components of the modal phase velocity $\mathbf{C}$, given by the shallow water dispersion relation

$$\mathbf{C} = (f/k)\,\mathbf{k}/k = \sqrt{gh}\,\mathbf{k}/k, \tag{9}$$

where k_x and κ are the cross-shore and alongshore components of the wavenumber vector $\mathbf{k}$, and satisfy $|\mathbf{k}|^2 = k^2 = \kappa^2 + k_x^2$.

[12] Up- and down-coast propagation in S_{PP} and S_{UU} are differentiated by the sign of κ, but shoreward and seaward propagating energy are not distinguished (S_{PP} and S_{UU} are symmetric in A_+ and A_-). However, $\mathcal{R}e\{S_{PU}\}$ is proportional to differences in shoreward and seaward energy fluxes ($|A_+|^2 - |A_-|^2$) (8), and equals the net cross-shore energy flux density in $\kappa - f$ space. The co-spectrum of collocated $p - u$ sensors is equal to the cross-shore energy flux at frequency f, integrated over κ. The integral of the $p - u$ co-spectra over all f is equal to the net flux (2).

[13] Combining (6)–(8) yields, at each f and κ, the variance density of shoreward and seaward propagating modes,

$$E_\pm = \frac{\mathsf{E}\left[\frac{1}{2}|A_\pm|^2\right]}{df d\kappa} = \frac{1}{4}\left(S_{PP} \pm \frac{h}{|C_x|} 2\mathcal{R}e\{S_{PU}\} + \frac{h^2}{C_x^2} S_{UU}\right) \tag{10}$$

and the corresponding cross-shore energy fluxes

$$F_\pm = \frac{h}{4}\left(\frac{|C_x|}{h} S_{PP} \pm 2\mathcal{R}e\{S_{PU}\} + \frac{h}{|C_x|} S_{UU}\right). \tag{11}$$

The variance (10) and flux (11) estimates are independent of the phase coupling between shoreward and seaward propagating components. The sense of alongshore and cross-shore propagation is given by the signs of κ and $F_\pm$. For example, F_+ with $\kappa > 0$ corresponds to shoreward and up-coast propagation. Alongshore energy fluxes in $\kappa - f$ space can be obtained by multiplying (10) by $|C_y|$. These results for long waves are readily extended using linear theory for finite depth.

[14] Gravity wave energy flux spectra can be estimated (using (11)) at locations where shear waves are energetic because shear and gravity wave energies are concentrated in different regions of $\kappa - f$ space. Shear waves propagate relatively slowly and satisfy $|\kappa| > \kappa_g$, where $\kappa_g = f/\sqrt{gh}$ is the theoretical maximum alongshore wavenumber for gravity waves [e.g., *Oltman-Shay et al.*, 1989; *Howd et al.*, 1991]. In contrast, shear waves degrade estimates of seaward and shoreward gravity wave fluxes (1) based on time or frequency domain analysis of collocated $p - u$ gauges (cases with energetic shear waves were excluded from *Sheremet et al.* [2002]).

[15] Waves incident from deep water onto a shelf with plane parallel contours maintain constant κ, where $0 < |\kappa| < 2\pi f^2/g$. Waves with $|\kappa|$ slightly less than $2\pi f^2/g$ propagate onto the shelf with highly oblique deep water angles, and waves with $\kappa \sim 0$ are approximately normally incident. If excited in shallow water, waves with $|\kappa| < 2\pi f^2/g$ can radiate (i.e., "leak") energy to deep water, reversing the ray path of waves incident from deep water, and are known as leaky waves [*Munk et al.*, 1964]. Waves with $|\kappa| > f^2/g$ cannot propagate in deep water, and if excited in shallow water, may undergo multiple, constructive reflections between the shoreline and an offshore turning point, where $\kappa = \kappa_g = \sqrt{gh}/f$. These are refractively trapped edge waves. Edge waves are trapped (e.g., have a turning point) shoreward of the array if $\kappa > \kappa_g$. The curves separating leaky from trapped waves ($\kappa = 2\pi f^2/g$), and separating edge waves trapped shoreward of the array from motions extending seaward of the array ($\kappa = \kappa_g$), are shown in Figure 3.

3. Application to Short Arrays

[16] At each frequency, spectral densities in κ space and cross-spectra (as observed with an alongshore array of sensors) form a Fourier pair, for example,

$$S_{PP}(\kappa) = \int_{-\infty}^{\infty} X_{PP}(\Delta) e^{-2\pi i \kappa \Delta} d\Delta,\ X_{PP}(\Delta) = \int_{-\infty}^{\infty} S_{PP}(\kappa) e^{2\pi i \kappa \Delta} d\kappa, \tag{12}$$

where Δ is the alongshore lag and X is the cross-spectrum. However, because the arrays usually deployed (e.g., Figure 1) are relatively short compared with the alongshore wavelengths of interest, a direct Fourier transform of observed cross-spectra yields $S(\kappa)$ with unacceptably low resolution. For example, in 4-m water depth with $f < 0.03$ Hz the alongshore wavelength of the shortest free gravity wave (e.g., the maximum gravity wavenumber $\kappa = \kappa_g = f/\sqrt{gh}$, indicated with a dashed line in Figure 3) is longer than the 200-m alongshore span of the array. (Shorter gravity waves with larger κ, for example mode zero, are trapped shoreward of the array.) Thus the lowest Fourier κ band contains the entire range of theoretically possible free gravity wave κ, including trapped and "leaky" waves incident from deep water [*Munk et al.*, 1964].

[17] Increased κ resolution requires additional assumptions that essentially extend the array length by extrapolating the observations. Widely used, "high-resolution" spectral estimators such as IMLE (Iterative Maximum Likelihood Estimator [*Pawka*, 1983]) and MEM (Maximum

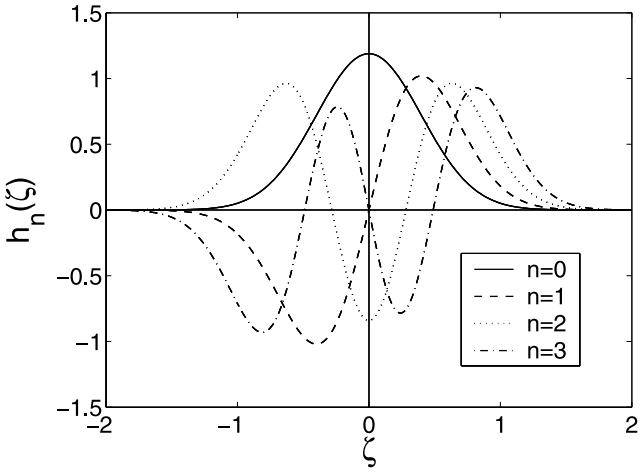

Figure 4. Hermite functions (A2) for $n \leq 3$.

Entropy Method, Figure 3a) are constrained to return positive-definite $S(\kappa)$ and thus are not useful for estimating $\mathcal{R}e\{S_{PU}\}$, that can have either sign.

[18] The alternative approach developed here is based on the assumption that the true cross-spectra decay at lags larger than those in the array, and that the true $S(\kappa)$ are smooth. The cross-spectra are expressed as a series of normalized Hermite functions, which form a complete and orthonormal basis [*Weaver*, 1989; *Folland*, 1992]. Hermite functions h_n of order n have a strongly localized oscillatory domain with n zero crossings separated by turning points from an outer region of rapid exponential decay (Figure 4). In addition to simple recursive properties, Hermite functions, like the Gaussian function (the lowest-order Hermite function), are self-reciprocal under the Fourier transform

$$\int_{-\infty}^{\infty} h_n(\Delta) e^{-2\pi i \kappa \Delta} d\Delta = (-i)^n h_n(\kappa), \tag{13}$$

simplifying considerably the procedure for finding solutions that satisfy simultaneously constraints in lag (fit the observed cross-spectra) and κ (smooth $S(\kappa)$) spaces.

[19] Since the estimate for $F_{\pm}$ (equation 11) uses only the real part of S_{PU} (S_{PP} and S_{UU} are real), only the Hermitian part of the observed cross-spectra is needed. The Hermitian part of $X = Co + iQu$, where Co and Qu are co- and quad-spectra, are approximated by sums of Hermite functions,

$$\begin{aligned} Co(\Delta_m) &= \sum_n c_n \mathbf{h}_n(\Delta_m/L) + \epsilon(\Delta_m), n = 0, 2, \ldots, 2(N-1) \\ Qu(\Delta_m) &= \sum_n c_n \mathbf{h}_n(\Delta_m/L) + \epsilon(\Delta_m), n = 1, 3, \ldots, 2N-1, \end{aligned} \tag{14}$$

where ϵ is the misfit, and L is a scale factor used to nondimensionalize the lag variable of the Hermite functions, and the index m identifies the alongshore spatial lag (there are M lags). Even and odd Hermite orders are used to represent the (even) co- and (odd) quad-spectra, and the number N of even and odd Hermite modes are equal.

[20] The finite number of cross-spectral observations can be fit closely with different sets of coefficients c_n (14), and some fits to the statistically noisy data result in wildly oscillating and nonphysical $S(\kappa)$. Following *Constable et al.* [1987] and *Herbers and Guza* [1990], the total "badness" of the solution is minimized by solving

$$\frac{\partial}{\partial c_j}\left(\alpha R + \boldsymbol{\epsilon}^{\mathbf{T}}\boldsymbol{\epsilon}\right) = 0, \tag{15}$$

where the badness $(\alpha R + \boldsymbol{\epsilon}^{\mathbf{T}}\boldsymbol{\epsilon})$ is the sum of a measure of the solution roughness αR, and the data misfit $\boldsymbol{\epsilon}^{\mathbf{T}}\boldsymbol{\epsilon}$ with $\boldsymbol{\epsilon}$ the column vector of misfits at different lags and the superscript $(\,)^{\mathbf{T}}$ denotes the transpose. Straightforward algebra yields an analytic expression ((A11) in Appendix A) for the roughness R, characterized as the norm of the second derivative of $S(\kappa)$ ((A1) in Appendix A). The Co or Qu spectra observed at M lags are fit with a given tolerance using N Hermite coefficients c_n that simultaneously minimize the roughness of the estimated $S(\kappa)$ (Appendix B). The contribution of Hermite mode n to the estimate roughness R grows roughly like n^2 (equation (A12) in Appendix A), so increasing the contribution of higher order Hermite modes improves the fit to the observed cross-spectra (e.g., decreases the misfit variance $\boldsymbol{\epsilon}^{\mathbf{T}}\boldsymbol{\epsilon}$), but increases R. Straightforward algebra yields a pair of equations for the coefficients c, for example, for Co,

$$\left[\mathbf{H}^{\mathbf{T}}\mathbf{H} + \alpha\mathbf{R}\right]\mathbf{c} = \mathbf{H}^{\mathbf{T}}\mathbf{Co}, \tag{16}$$

where $\mathbf{c}$ is the column vector (dimension N) of Hermite coefficients, and $\mathbf{Co}$ is the column vector (dimension M) of observed co-spectral values (14). The matrix $\mathbf{H}$ (dimension $N \times M$) has elements

$$[\mathbf{H}]_{lm} = h_n(\Delta_m/L), \tag{17}$$

where (from (14)) $n = 2(l-1)$ for co-spectra and $n = 2l-1$ for quad-spectra. The roughness matrix $\mathbf{R}$ (dimension $N \times N$),

$$R = \mathbf{c}^{\mathbf{T}}\mathbf{R}\mathbf{c}, \tag{18}$$

(R is given in (A11)) has elements

$$[\mathbf{R}]_{li} = \frac{q_k}{q_{k-4}}\delta_{n,k-4} + \frac{q_k}{q_{k-2}}\delta_{n,k-2} + \left[\frac{q_k^2}{q_{k-2}^2} + (2k+1)^2 + \frac{q_{k+2}^2}{q_k^2}\right]\delta_{n,k} + \frac{q_{k+2}}{q_k}\delta_{n,k+2} + \frac{q_{k+4}}{q_k}\delta_{n,k+4}, \tag{19}$$

where $q_n^2 = n!$, and for cospectra $n = 2(l-1)$ and $k = 2(i-1)$, and for quad-spectra $n = 2l-1$ and $k = 2i-1$ (14).

[21] Equations (16), (17), and (19) form the basis of the method. Equation (16) can be solved using singular value decomposition methods [*Strang*, 1988] to obtain the coefficients c_n of the decomposition (14) of the observed X_{PP}, X_{UU}, and X_{PU}. From the self-reciprocity (13), the decomposition coefficients of the corresponding spectra (the Fourier transform of the cross-spectrum 12) are $(-i)^n c_n$,

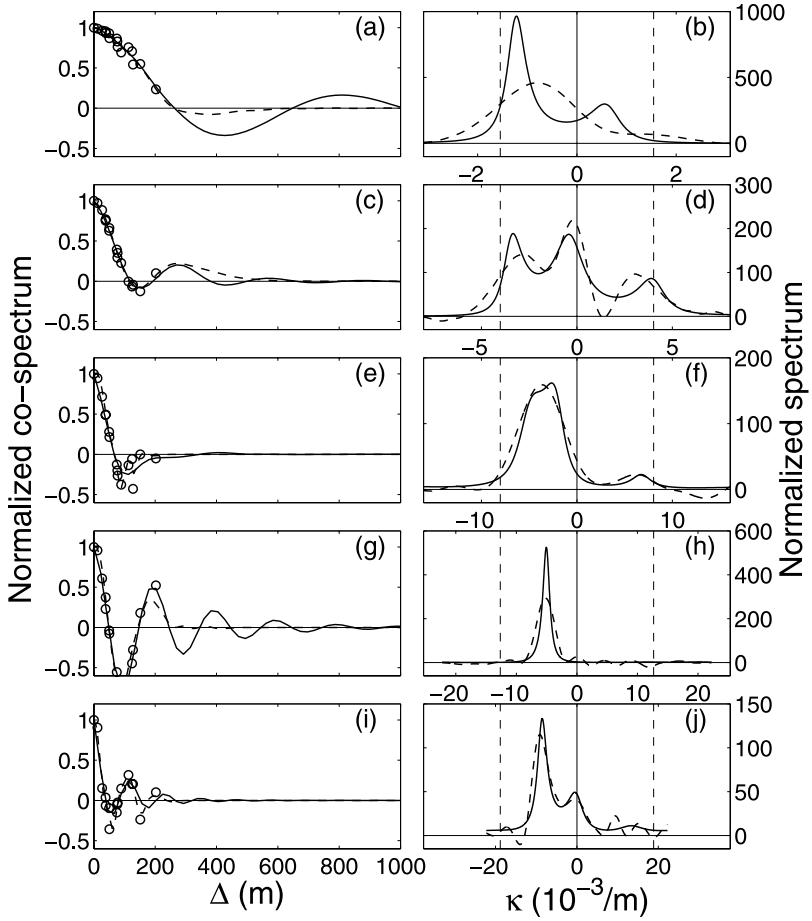

Figure 5. Comparison of MEM (solid curves) and Hermite (dashed curves) estimators at x = 260 m at frequencies (a, b) 0.01, (c, d) 0.025, (e, f) 0.05, (g, h) 0.08 (spectral peak), and (i, j) 0.12 Hz. (left) Estimated pressure co-spectra X_{PP} versus alongshore lag Δ (observations are shown as circles). Quad-spectrum estimates show similar features. (right) Estimated $\kappa - f$ spectra S_{PP} of pressure. The spectra are normalized to unit area, integrated over κ. Dashed vertical lines mark the turning-point limits of the WKB validity domain ($|\kappa| = f/\sqrt{gh}$). Note that the κ scales vary by a factor of 10 between Figures 5b and 5j.

so estimates of the corresponding ($\kappa - f$) densities S_{PP}, S_{UU} and S_{PU} are readily available. For example,

$$S_{PU}(\kappa L) = \sum_{k=0}^{N-1} (-1)^k [c_{2k}\mathbf{h}_{2k}(\kappa L) + c_{2k+1}\mathbf{h}_{2k+1}(\kappa L)]. \quad (20)$$

With S_{PP}, S_{UU} and S_{PU} known, equation (11) provides the four-quadrant cross-shore fluxes.

[22] The scale factor L (17) maps the dimensional lag space observations into the space of the nondimensional Hermite variable. For each frequency the optimal values of L and the trade-off parameter α (15) are defined as those yielding, with a fixed number of Hermite modes, the Hermite-based κ-spectrum with minimum roughness that fits the observed cross-spectra with a given error (Appendix B). Results are not sensitive to the number of Hermite modes (here, N = 15), nor to details of the procedure for selecting L and α.

4. Results

[23] MEM estimates are positive, so MEM cannot be used to estimate S_{PU}, or energy flux spectra that depend on S_{PU} (11). MEM and Hermite estimates of S_{PP} are qualitatively similar at all frequencies (infragravity frequencies are shown in Figure 3). The cross-spectra associated with both MEM and Hermite estimates fit the observed cross-spectra closely (Figure 5, left), so their differences (Figure 5, right) reflect how each estimator resolves uncertainty (both statistical and arising from the limited array length) inherent in the basic cross-spectral observations. The estimates differ most at the lowest frequency (Figure 5b) because the long wavelength motions (Figure 5a) severely limit the array resolution. The MEM estimate is narrower than the Hermite-based estimate, reflecting the different properties of each method: high peak resolution in MEM and estimated smoothness in the present method. The estimate similarity increases at higher frequencies because the shorter wavelengths are better constrained by the observations, decreasing the importance of differences in the estimator extrapolations.

[24] Example full (four-quadrant) cross-shore energy flux density spectra (Figures 6–8) are shown at the alongshore array located x = 260 m (in about 4-m depth) for three 3-hour runs with much different incident sea-swell significant heights (in 8-m water depth, about 1 km offshore, $H_{sig,8m}$ =

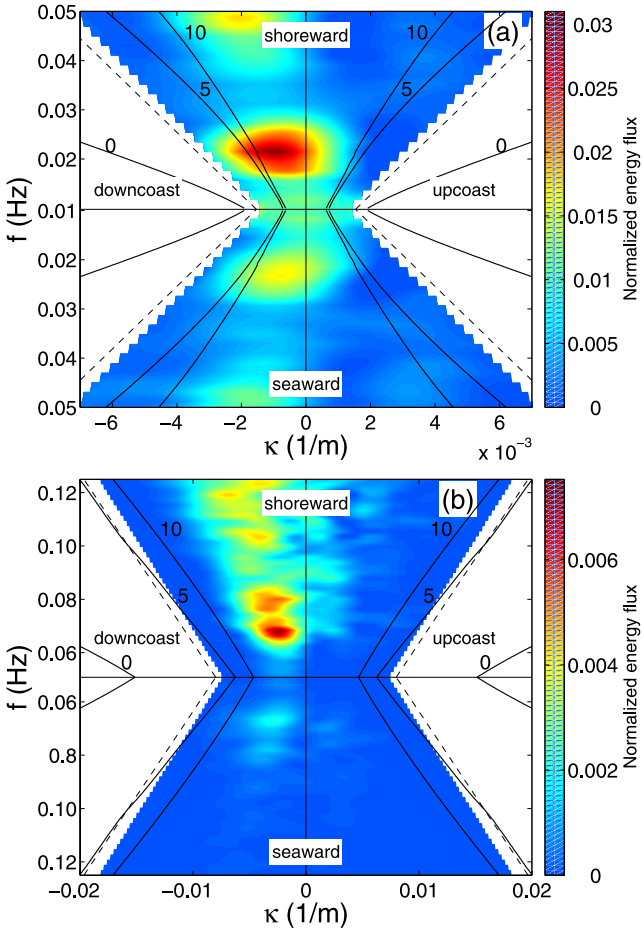

Figure 6. Cross-shore energy flux density in $\kappa - f$ space at x = 260 m, for 15 August 1997, 0100–0400 EST for (a) infragravity and (b) sea-swell frequencies. Edge wave dispersion curves for modes 0, 5, and 10 are solid curves, and dashed lines are the limit of validity for the WKB approximation ($|\kappa| = \kappa_g = f/\sqrt{gh}$). Densities are normalized by the total shoreward flux (sea swell and infragravity fluxes are 2.6 $\times$ 10^4 and 5.8 $\times$ 10^2 cm^3/s, respectively) so the integrated shoreward flux is 1.0, and the integrated seaward flux is R^2. The maximum color scale value is determined by the maximum normalized density. In Figures 6a and 6b, at fixed f, seaward and shoreward fluxes have maxima at similar κ, consistent with specular reflection.

0.3, 0.9, and 1.7 m for 15 August, 10 September, and 17 October, respectively (Table 1). The observed cross-shore variation of sea-swell energy fluxes (similar to Figure 2a) suggests that the array at x = 260 m is located many surfzone widths offshore, near the outer edge of the surfzone, and in the inner surfzone, respectively. On 15 August and 10 September, wave breaking seaward of the array is minimal, and the wave height observed at the array in 4-m depth $H_{sig,4m}$ is slightly greater than $H_{sig,8m}$, whereas breaking reduces $H_{sig,4m}$ on 17 October to 1.1 m, only slightly larger than H_{sig} = 1.0 m on 10 September (Table 1). In all cases, shoreward propagating sea and swell is strongly dissipated in the surfzone shoreward of the array. The seaward sea-swell flux is less than 3% of the seaward sea-swell flux at the array on 10 September and 17 October (Figures 7b and 8b). Stronger reflection, ~10%, is observed on 15 August (Figure 6b) with small incident waves at high tide, when the water line intersects a steep portion of the beach face, consistent with previous observations at this site obtained with a two-dimensional array of pressure sensors in 13m water depth [*Elgar et al.*, 1994].

[25] At infragravity frequencies, the flux reflection coefficient R^2_{ig} (ratio of seaward to shoreward fluxes) is influenced by generation shoreward of the array, as well as dissipation occurring during both propagation and shoreline reflection [*Herbers et al.*, 1995a, 1995b]. If, onshore of the array, generation exceeds dissipation, then $R^2_{ig} > 1$, whereas if dissipation exceeds generation, $R^2_{ig} < 1$.

[26] Estimates of four-quadrant infragravity energy flux allow calculation of the $\kappa - f$ distribution of the flux reflection coefficient. To avoid spurious reflection values at $\kappa - f$ where fluxes are low and the estimates are inaccurate, and to increase the statistical stability of the estimates, fluxes are integrated over each of the $\kappa - f$ regions of elevated shoreward flux. Seaward fluxes are integrated over the same regions of $\kappa - f$ space consistent with the observed specular reflection. For example, on

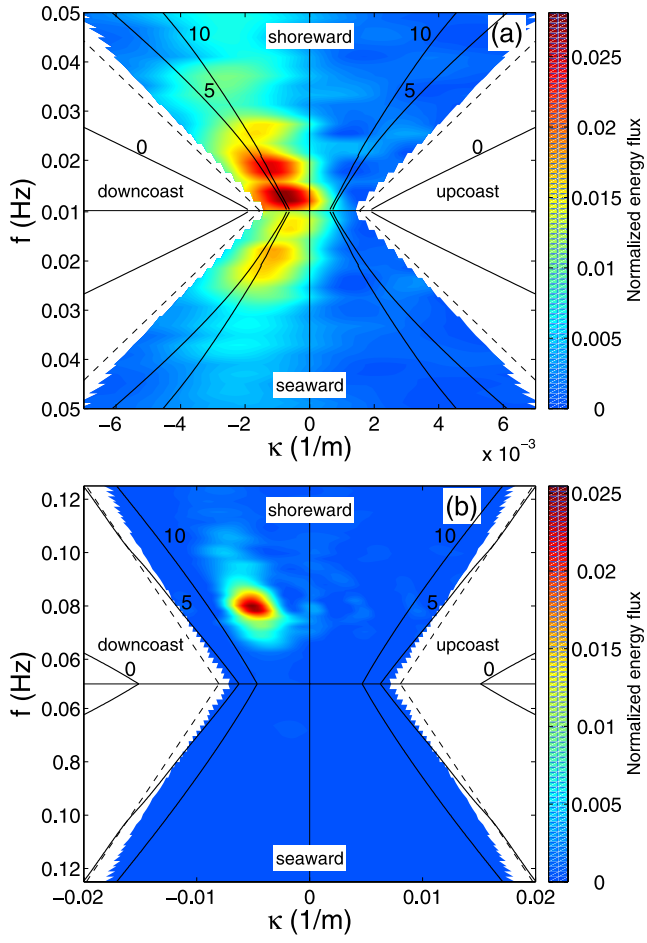

Figure 7. Cross-shore energy flux density in $\kappa - f$ space at x = 260 m, for 10 September 1997, 0100–0400 EST for (a) infragravity and (b) sea-swell frequencies. Densities are normalized by the total shoreward flux (sea swell and infragravity fluxes are 3.4 $\times$ 10^5 and 1.4 $\times$ 10^4 cm^3/s, respectively). Figure is same format as Figure 6.

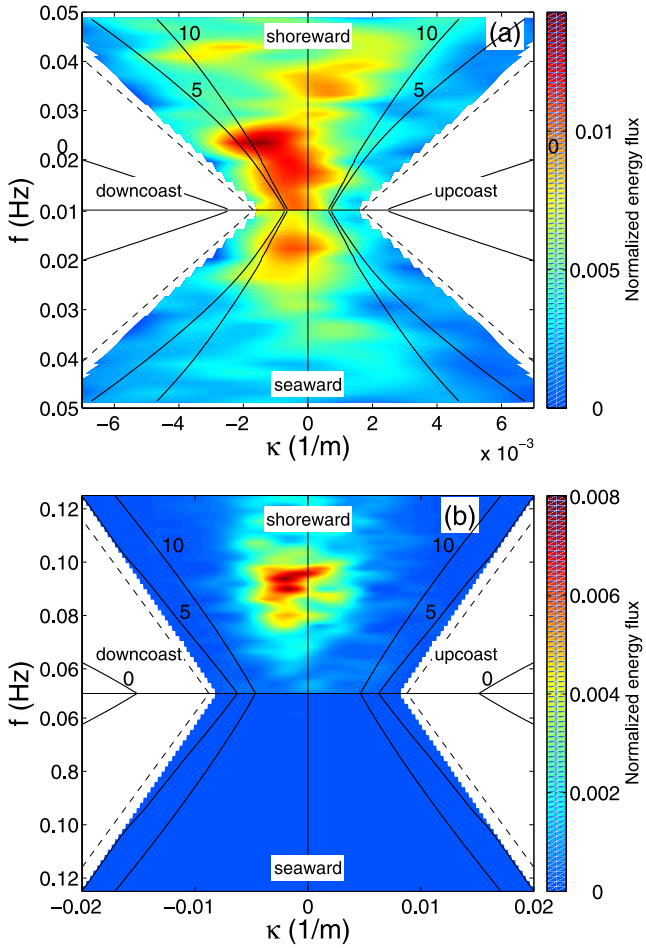

Figure 8. Cross-shore energy flux density in $\kappa - f$ space at x = 260 m, for 17 October 1997, 0100–0400 EST for (a) infragravity and (b) sea-swell frequencies. Densities are normalized by the total shoreward flux (sea swell and infragravity fluxes are 4.2 × 10^5 and 1.8 × 10^4 cm^3/s, respectively). Figure is same format as Figure 7.

10 September, R^2_{ig} are between about 0.3 and 0.6 for frequency bands centered at f = 0.013, 0.019, 0.028, and 0.040 Hz (Figure 7). Flux spectra at other alongshore arrays also show negligible sea-swell reflection, and suggest specular, partial reflection of infragravity waves.

[27] The other case examples have $H_{sig,8m}$ about a factor of 2 larger (17 October) and smaller (15 August) than on 10 September. In all three cases, infragravity wave reflection is specular and incomplete. On 17 October, the large sea-swell waves are closer to normal incidence than on 10 September (i.e., the energy maxima is closer to κ = 0) and so are the infragravity waves (compare Figure 8 with Figure 7). The $R^2_{ig} \sim 0.5$ are similar (Table 1). With the smallest waves (10 September), $R^2_{ig} \sim 0.7$ is higher, but dissipation is still significant. Edge wave growth is apparently suppressed by significant dissipation within a wave cycle, supporting earlier work by *Henderson and Bowen* [2002, 2003]. Results from these case examples and the entire data set will be explored further elsewhere.

5. Discussion

[28] The WKB-based estimator (6–8) assumes that gravity waves, either leaky or refractively trapped, dominate the motions observed in the band $|\kappa| < \kappa_g = f/\sqrt{gh}$. In the WKB approximation, observed alongshore velocities are theoretically redundant with p and u,

$$S_{VV} = \frac{C_y^2}{h^2} S_{PP}, \quad S_{PV} = \frac{C_y}{h} S_{PP}, \quad S_{UV} = \frac{C_y}{h} S_{PU}. \qquad (21)$$

Estimates of S_{VV} based directly on v, and on p measurements using (21), are similar (Figures 9a, 9b, 9d, and 9e), as are the corresponding v energy spectra (Figures 9c and 9f, estimated by integrating S_{VV} over κ), supporting the underlying assumptions. Differences are largest at infragravity frequencies (Figures 9a and 9b), where the directly measured S_{VV} (Figure 9a) is less concentrated along $\kappa = \kappa_g$ than the estimate based on the measured S_{PP} and WKB theory. The present WKB-based theory is problematic when $\kappa \sim \kappa_g$ and cross-shore flux estimates are not shown near the dashed curve in Figures 6–8. However, directly measured infragravity pressure spectra S_{PP}, estimated without WKB theory, usually have maxima at $\kappa < \kappa_g$ and relatively low energy when $\kappa \geq \kappa_g$ (Figure 3). Considering all the arrays operational during the three case example runs, the variance with $\kappa \geq \kappa_g$ accounts for an average of 7% and a maximum of 9% of the total pressure variance (integrated over κ and infragravity f).

[29] The WKB relationship between p and u (6–8), critical to the estimator, is based on the assumption of slowly varying depth, with the wave amplitude given by energy conservation and the wavenumber by constant-depth solutions. The linear shallow water equations relax the slowly varying assumption, and the bottom slope appears explicitly. Comparison of WKB wavenumbers and amplitudes with those obtained numerically from the shallow water equations for a normally incident shoreward progressive wave (Figure 10) indicates less than 10% error in WKB theory for all frequencies considered here (f > 0.01 Hz)

Table 1. Wave Characteristics for the Case Examples, Measured at the FRF Array in 8-m Depth, and in About 4-m Depth at x = 260 m[a]

Run, Eastern Standard Time	$H_{sig,8m}$ Sea Swell, m	$H_{sig,4m}$ Sea Swell, m	$H_{sig,4m}$ Infragravity, m	$u_{rms,4m}$ Sea Swell, m/s	$u_{rms,4m}$ Infragravity, m/s	R^2_{ig} Infragravity
15 August 1997, 0100–0400	0.3	0.3	0.06	0.1	0.03	0.7
10 September 1997, 0100–0400	0.9	1.0	0.3	0.4	0.1	0.5
17 October 1997, 0100–0400	1.7	1.1	0.3	0.5	0.2	0.5

[a]See Figure 1. Estimates of the significant wave height H_{sig}, root-mean square velocity fluctuation u_{rms}, and flux reflection coefficient R^2 are based on band-passed time series (infragravity 0.01–0.05 Hz, sea swell 0.05–0.33 Hz).

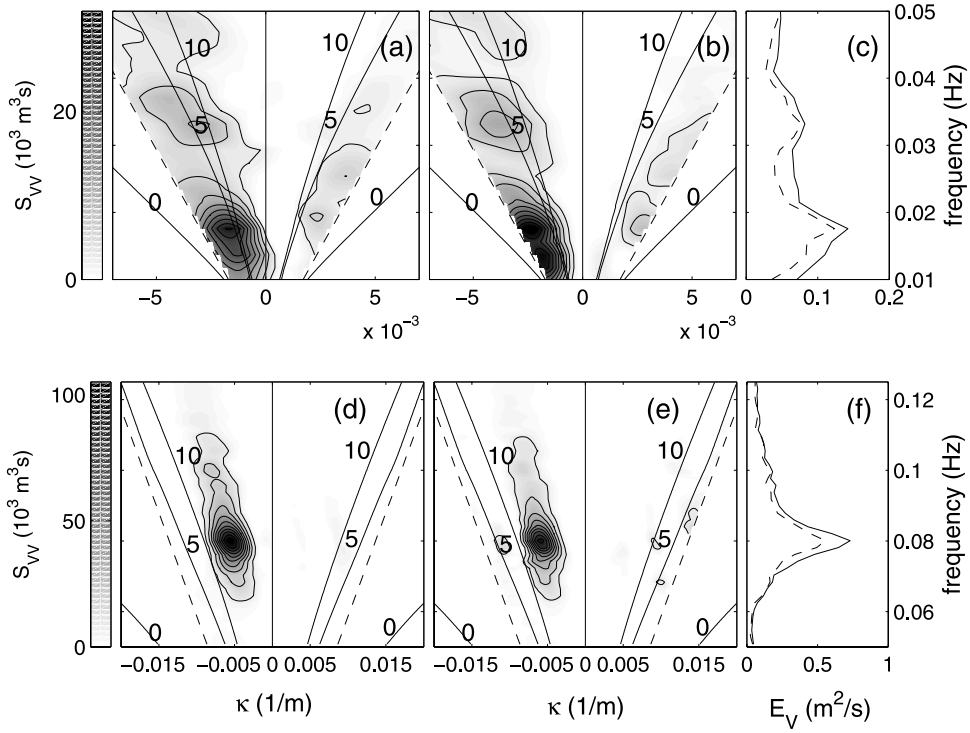

Figure 9. Alongshore velocity $\kappa - f$ spectra S_{VV} at $x = 260$ m for 10 September (estimated using Hermite transforms) based on (a, d) v cross-spectra, and (b, e) p cross-spectra (WKB theory, $S_{PP}\, C_y^2/h^2$, (21)), for (top) infragravity and (bottom) sea-swell frequencies. Solid curves are edge wave dispersion relations for modes 0, 5, and 10, and dashed curves define turning points in the WKB approximation ($|\kappa| = \kappa_g = f/\sqrt{gh}$). Results are shown for ($|\kappa| < f/\sqrt{gh}$). (c, f) Alongshore velocity frequency spectra E_v at $x = 260$ m estimated by integrating (over $|\kappa| < f/\sqrt{gh}$) S_{VV} (Figures 9a and 9d) and $S_{PP}C_y^2/h^2$ (Figures 9b and 9e) (solid and dashed lines, respectively).

for $x > 210$ m, and for $f > 0.022$ Hz at the shallowest alongshore array ($x = 160$ m).

6. Summary

[30] A new method for estimating wave energy fluxes from array observations is described. Under the WKB approximation, pressure and cross-shore velocity measured on an alongshore-oriented transect yield the distribution of onshore and offshore energy fluxes in alongshore wavenumber-frequency space. Preliminary analysis of data from the spatially sparse and relatively short SandyDuck arrays shows that dissipation of shoreward propagating infragravity waves occurs over a wide range of alongshore wavenumbers, including those of (theoretically) refractively trapped edge waves.

Appendix A: Roughness

[31] We derive an exact analytic expression for the roughness R of the $f - k_y$ spectrum $S(f, \kappa)$. The analytical form greatly simplifies the solution of the equations for the coefficients c_n.

[32] The roughness of $S(f,\kappa)$ is [*Constable et al.*, 1987]

$$R(f) = \int_{-\infty}^{\infty} \left| \frac{d^2 S(f,\kappa)}{d\kappa^2} \right|^2 d\kappa. \tag{A1}$$

Hermite functions of mode n are [*Weaver*, 1989]

$$\overline{h}_n(t) = \left(\frac{-1}{\sqrt{4\pi}}\right)^n e^{\pi t^2} \frac{d^n}{dt^n}\, e^{-2\pi t^2}, \tag{A2}$$

with the first four modes

$$\overline{h}_0(t) = e^{-\pi t^2}, \quad \overline{h}_1(t) = \sqrt{4\pi}\, t\, e^{-\pi t^2}, \; \overline{h}_2(t) = \left(4\pi\, t^2 - 1\right) e^{-\pi t^2}$$
$$\overline{h}_3(t) = \left\{ \left[\sqrt{4\pi}\, t\right]^3 - \sqrt{4\pi}\, t \right\} e^{-\pi t^2} \tag{A3}$$

and the recursive relation

$$\overline{h}_{n+1}(t) = 2\sqrt{\pi}\, t\, \overline{h}_n(t) - n\overline{h}_{n-1}(t), \tag{A4}$$

where $\overline{h}_j = 0$, $j < 0$.

[33] Hermite functions are also solutions of the Sturm-Liouville differential equation

$$\overline{h}_n''(t) = 2\pi\left[2\pi t^2 - (2n+1)\right]\overline{h}_n(t), \tag{A5}$$

where $\overline{h}_n''$ is the second derivative of Hermite mode n. Combining (A4) and (A5) yields

$$\overline{h}_n'' = \pi\left[\overline{h}_{n+2} - (2n+1)\overline{h}_n + n(n-1)\overline{h}_{n-2}\right]. \tag{A6}$$

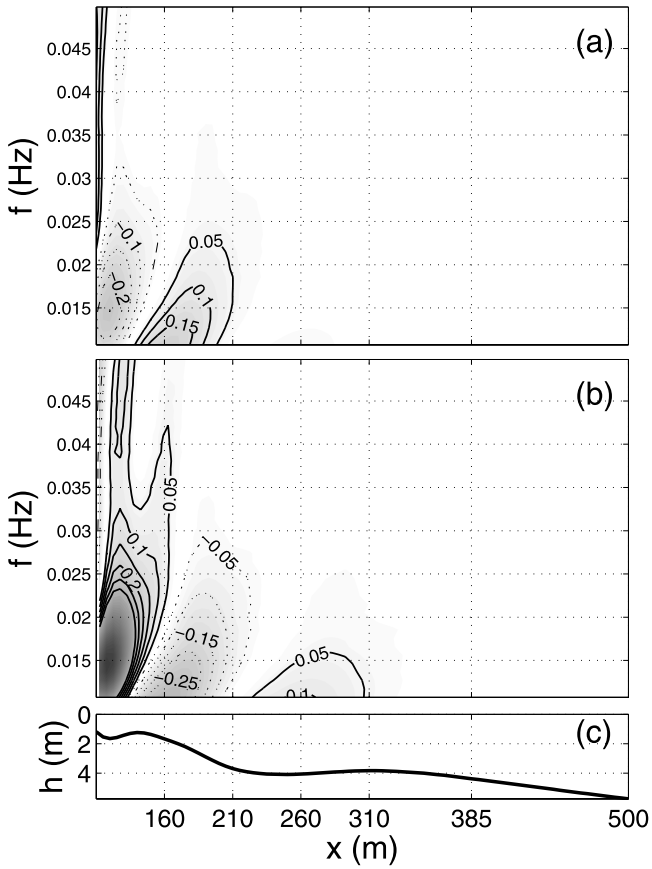

Figure 10. Contours of fractional errors in WKB estimates of (a) amplitude and (b) wavenumber based on comparison with exact solutions to the linear shallow water equations for a shoreward propagating, normally incident wave using (c) depth h versus cross-shore coordinate x observed on 10 September.

Using

$$\int_{-\infty}^{\infty} \overline{h}_n^2 dt = \frac{n!}{\sqrt{2}} \tag{A7}$$

to normalize, the set of orthonormal Hermite functions is

$$h_n = \frac{\sqrt[4]{2}}{\sqrt{n!}}\,\overline{h}_n, \quad \text{with} \quad \int_{-\infty}^{\infty} h_n(t)h_m(t)dt = \delta_{m,n}, \tag{A8}$$

where δ is the Kronecker symbol.

[34] Using (13), the Fourier transform $g(t)$ of a function G decomposed into Hermite functions $G = \Sigma c_n h_n$ is

$$g(t) = \sum_{n=1}^{\infty} (-i)^n c_n h_n(t). \tag{A9}$$

The roughness (A1) is

$$R = \int_{-\infty}^{\infty} g''(t)[g''(t)]^* dt, \tag{A10}$$

where the superscript asterisk denotes complex conjugate. After some straightforward algebra using (A2)–(A6),

$$R = \pi^2 \sum_n c_n \left\{ \frac{q_n}{q_{n-4}}\, c_{n-4} + \frac{q_n}{q_{n-2}} c_{n-2} + \left[\frac{q_n^2}{q_{n-2}^2} + (2n+1)^2 + \frac{q_{n+2}^2}{q_n^2} \right] c_n + + \frac{q_{n+2}}{q_n}\, c_{n+2} + \frac{q_{n+4}}{q_n} c_{n+4} \right\}, \tag{A11}$$

where $q_n^2 = n!$, the range of n is given by (14), and terms vanish if they contain q_n or c_n with negative n. For example,

$$q_n/q_{n-4} = \begin{cases} \sqrt{n(n-1)(n-2)(n-3)}, & \text{for } n \geq 4 \\ 0, & \text{otherwise.} \end{cases} \tag{A12}$$

Appendix B: Parameters α and L

[35] The scale factor L (B1) maps the dimensional lag space observations into the nondimensional Hermite variable space (14). Optimal values of L match the spatial scales of Hermite functions and the observed cross-spectra, and thus fit the observations efficiently (e.g., using low modes with low roughness). Values of L that are too large squeeze the entire lag domain of the observations into a small interval near the Hermite origin, and too small values spread the observed lag domain far out into the Hermite exponential decay region (Figure 4). Here L is related to a fixed point characterizing the Hermite functions, the turning point $t_T \simeq 0.40$ of the Gaussian $h_0(t)$, and the maximum lag Δ_M,

$$L = s\frac{\Delta_M}{t_T}, \tag{B1}$$

where s is the fraction of Δ_M mapped into the Hermite interval $[0, t_T]$. A typical value of $s = 0.4$ yields $\Delta_M/L = 2.5t_T \simeq 1$; that is, in (14) the observed cross-spectra are fit with Hermite functions spanning the range $t \leq 1$ (see Figure 4).

[36] For simplicity, for each frequency the optimal values of s (and hence L) and the tradeoff parameter α (15) are defined as those yielding the Hermite-based κ-spectrum with minimum roughness and fitting the observed cross-spectra within a given error. More rigorous approaches, based on the statistical confidence level of the fit [*Long and Hasselmann*, 1979], are more complex and require estimates of the error-covariance matrix. Optimal (s, α) values were found for each cross-spectral combination of p and u, at each array, and each frequency. Large α values have smooth $S(\kappa)$ but large misfit (15). For a given s, the optimal α (denoted α_s) is the maximum value of α (e.g., smoothest $S(\kappa)$) for which the misfit is within 1% of the cross-spectral norm. For a given frequency, the optimal (minimum roughness) solution is found by searching (s, α_s) pairs over s in the interval of [0.1–10]. Optimal values of s are usually between 0.1 and 0.6, and are frequency dependent, with the largest values (and hence smallest Δ_M/L) at low frequency where the observed cross-spectra are most slowly varying (i.e., spatial scales are longest).

[37] **Acknowledgments.** Funding was provided by the Office of Naval Research, the National Science Foundation, and the National Oceanographic Partnership Program (NOPP) program. Steve Elgar and Britt Raubenheimer contributed substantially to all aspects of the Sandy-Duck field program.

References

Battjes, J. A., H. J. Bakkenes, T. T. Janssen, and A. R. van Dongeren (2004), Shoaling of subharmonic gravity waves, *J. Geophys. Res.*, *109*, C02009, doi:10.1029/2003JC001863.

Constable, S., R. L. Parker, and C. Constable (1987), Occam's inversion: A practical algorithm for generating smooth models from electromagnetic sounding data, *Geophysics*, *52*(3), 289–300.

Elgar, S., and R. T. Guza (1985), Observations of bispectra of shoaling surface gravity waves, *J. Fluid Mech.*, *161*, 425–448.

Elgar, S., T. H. C. Herbers, and R. T. Guza (1994), Reflection of ocean surface gravity waves from a natural beach, *J. Phys. Oceanogr.*, *24*(7), 1503–1511.

Elgar, S., R. T. Guza, W. C. O'Reilly, B. Raubenheimer, and T. H. C. Herbers (2001), Observations of wave energy and directions near a pier, *J. Waterw. Port Coastal Ocean Eng.*, *127*, 2–6.

Feddersen, F., R. T. Guza, S. Elgar, and T. H. C. Herbers (2000), Velocity moments in alongshore bottom stress parameterizations, *J. Geophys. Res.*, *105*, 8673–8686.

Folland, G. B. (1992), *Fourier Analysis and Its Applications*, Wadsworth, Stamford, Conn.

Gallagher, B. (1971), Generation of surf beat by non-linear wave interactions, *J. Fluid Mech.*, *49*, 1–20.

Guza, R. T., E. B. Thornton, and R. A. Holman (1984), Swash on steep and shallow beaches, paper presented at 19th Coastal Engineering Conference, Am. Soc. of Civ. Eng., Houston, Texas.

Henderson, S. M., and A. J. Bowen (2002), Observations of surf beat forcing and dissipation, *J. Geophys. Res.*, *107*(C11), 3193, doi:10.1029/2000JC000498.

Henderson, S. M., and A. J. Bowen (2003), Simulations of dissipative, shore-oblique infragravity waves, *J. Phys. Oceanogr.*, *33*, 1722–1732.

Herbers, T. H. C., and R. T. Guza (1990), Estimation of directional wave spectra from multi-component observations, *J. Phys. Oceanogr.*, *20*, 1703–1724.

Herbers, T. H. C., S. Elgar, and R. T. Guza (1995a), Infragravity frequency (0.005–0.05 Hz) motions on the shelf: II. Free waves, *J. Phys. Oceanogr.*, *25*, 1063–1079.

Herbers, T. H. C., S. Elgar, and R. T. Guza (1995b), Generation and propagation of infragravity waves, *J. Geophys. Res.*, *100*, 24,863–24,872.

Howd, P. A., J. Oltman-Shay, and R. A. Holman (1991), Wave variance partitioning in the trough of a barred beach, *J. Geophys. Res.*, *96*, 12,781–12,795.

Huntley, D. A., R. T. Guza, and E. B. Thornton (1981), Field observations of surf beat: 1. Progressive edge waves, *J. Geophys. Res.*, *86*, 6451–6466.

Isobe, M., and K. Kondo (1984), Method for estimating directional wave spectrum in incident and reflected wave field, paper presented at 19th Coastal Engineering Conference, Am. Soc. of Civ. Eng., Houston, Texas.

Janssen, T., and A. Battjes (2003), Long waves induced by short-wave groups over a sloping bottom, *J. Geophys. Res.*, *108*(C8), 3252, doi:10.1029/2002JC001515.

List, J. H. (1992), A model for the generation of two-dimensional surf beat, *J. Geophys. Res.*, *97*, 5623–5636.

Long, R. B., and K. Hasselmann (1979), A variational technique for extracting directional spectra from multi-component wave data, *J. Phys. Oceanogr.*, *9*, 373–381.

Longuet-Higgins, M. S., and R. W. Stewart (1962), Radiation stress and mass transport in surface gravity waves with application to "surf beats," *J. Fluid Mech.*, *13*, 481–504.

Munk, W. H. (1949), Surf beat, *Eos Trans. AGU*, *30*, 849–854.

Munk, W., F. Snodgrass, and F. Gilbert (1964), Long waves on the continental shelf: An experiment to separate trapped and leaky modes, *J. Fluid Mech.*, *20*, 529–553.

Oltman-Shay, J., and R. T. Guza (1987), Infragravity edge wave observations on two California beaches, *J. Phys. Oceanogr.*, *17*, 644–663.

Oltman-Shay, J., P. Howd, and W. Birkemeier (1989), Shear instabilities of the mean longshore current: 2. Field observations, *J. Geophys. Res.*, *94*, 18,031–18,042.

Pawka, S. (1983), Island shadows in wave directional spectra, *J. Geophys. Res.*, *88*, 2579–2591.

Reniers, A., A. van Dongeren, J. Battjes, and E. Thornton (2002), Linear modeling of infragravity waves during Delilah, *J. Geophys. Res.*, *107*(C10), 3137, doi:10.1029/2001JC001083.

Ruessink, B. G. (1998), Bound and free infragravity waves in the nearshore zone under breaking and non-breaking conditions, *J. Geophys. Res.*, *103*, 12,795–12,805.

Sheremet, A., R. T. Guza, S. Elgar, and T. H. C. Herbers (2002), Observations of nearshore infragravity waves: Seaward and shoreward propagating components, *J. Geophys. Res.*, *107*(C8), 3095, doi:10.1029/2001JC000970.

Stoker, J. J. (1947), *Water Waves*, Wiley-Intersc., Hoboken, N. J.

Strang, G. (1988), *Linear Algebra and Its Applications*, 3rd ed., Harcourt Brace, San Diego, Calif.

Suhayda, J. N. (1974), Standing waves on beaches, *J. Geophys. Res.*, *79*, 3065–3071.

Van Dongeren, A., A. Reniers, J. Battjes, and I. Svendsen (2003), Numerical modeling of infragravity wave response during DELILAH, *J. Geophys. Res.*, *108*(C9), 3288, doi:10.1029/2002JC001332.

Weaver, H. J. (1989), *Theory of Discrete and Continuous Fourier Analysis*, John Wiley, Hoboken, N. J.

Wu, N. (1997), *The Maximum Entropy Method*, Springer-Verlag, New York.

R. T. Guza, Integrative Oceanography Division, Scripps Institution of Oceanography, University of California, San Diego, La Jolla, CA 92093-0209, USA. (rguza@ucsd.edu)

T. H. C. Herbers, Department of Oceanography, Naval Postgraduate School, Monterey, CA 93943-5122, USA. (thherber@nps.edu)

A. Sheremet, Coastal Studies Institute, Louisiana State University, Baton Rouge, LA 70803, USA. (ashere1@lsu.edu)